nanomaterials

MDPI

Article

Tandem Structures Semiconductors Based on TiO_2_SnO_2 and ZnO_SnO_2 for Photocatalytic Organic Pollutant Removal

Alexandru Enesca [1,*] and Luminita Isac [2]

[1] Product Design, Mechatronics and Environmental Department, Transilvania University of Brasov, Eroilor 29 Street, 35000 Brasov, Romania
[2] Renewable Energy Systems and Recycling Research Center, Transilvania University of Brasov, Eroilor 29 Street, 35000 Brasov, Romania; isac.luminita@unitbv.ro
* Correspondence: aenesca@unitbv.ro

Abstract: The photocatalyst materials correlation with the radiation scenario and pollutant molecules can have a significant influence on the overall photocatalytic efficiency. This work aims to outline the significance of optimizing the components mass ratio into a tandem structure in order to increase the photocatalytic activity toward pollutant removal. ZnO_SnO_2 and TiO_2_SnO_2 tandem structures were obtained by the doctor blade technique using different mass ratios between the components. The samples contain metal oxides with crystalline structures and the morphology is influenced by the main component. The photocatalytic activity was tested using three radiation scenarios (UV, UV-Vis, and Vis) and two pollutant molecules (tartrazine and acetamiprid). The results indicate that the photocatalytic activity of the tandem structures is influenced by the radiation wavelength and pollutant molecule. The TiO_2_SnO_2 exhibit 90% photocatalytic efficiency under UV radiation in the presence of tartrazine, while ZnO_SnO_2 exhibit 73% photocatalytic efficiency in the same experimental conditions. The kinetic evaluation indicate that ZnO_SnO_2 (2:1) have a higher reaction rate comparing with TiO_2_SnO_2 (1:2) under UV radiation in the presence of acetamiprid.

Keywords: metal oxides; doctor blade; tandem structures; photocatalysis; kinetics

Citation: Enesca, A.; Isac, L. Tandem Structures Semiconductors Based on TiO_2_SnO_2 and ZnO_SnO_2 for Photocatalytic Organic Pollutant Removal. *Nanomaterials* **2021**, *11*, 200. https://doi.org/10.3390/nano11010200

Received: 23 December 2020
Accepted: 12 January 2021
Published: 14 January 2021

1. Introduction

The semiconductor-mediated photocatalysis is considered as a promising pathway of removing various pollutants from aqueous and gaseous phase by directly harvesting and utilizing the solar energy [1–3]. Merging the sustainability with durability may be the key of transferring the photocatalytic process from the laboratory scale up to large applications. Until now there are many wide gap oxides (TiO_2 [4,5], SnO_2 [6,7], and ZnO [8,9]) and narrow band gap materials (Bi_2WO_6 [10,11], Ag_3PO_4 [12,13], $BiPO_4$ [14,15], g-C_3N_4 [16,17], WO_3 [18,19], and BiOX [20,21]) studied for the potocatalytic removal of wastewater organic contaminants and indoor pollutants. The mono-components photocatalyst have disadvantages such as narrow visible light absorption [22,23], low specific surface area [24,25], and fast charge carriers recombination [26,27].

Advanced oxidation processes (AOPs) are considered as future alternative to traditional methods of removing organic pollutants: pharmaceutical active compounds [28,29], pesticides [30,31], dyes [32,33], volatile organic compounds [34,35], etc. The sustainability represents an important advantage of AOPs due to the use of light radiation as the main energy source to provide oxidative species responsible for pollutant mineralization [36–38]. However, the transfer from a laboratory scale to a large application requires important optimizations in terms of energy consumption, materials, and design [39,40]. The lack of standardizations and procedures make it difficult to compare the experimental results reported in the field of photocatalysis. However, it must be underlined that the photocatalytic efficiency depends on many parameters such as pollutant type and concentration, photocatalyst composition, structure and dosage, as well as radiation wavelength and

photon flux. Bi_2MoO_6/Fe_3O [41] and $Ta_3B_2@Ta_2O_5$ [42] heterostructures were employed to investigate methylene blue (MB) dye removal under Vis irradiation. The results indicate that Bi_2MoO_6/Fe_3O_4 heterostructure have 93% photocatalytic efficiency after 180 min of irradiation with 500 W light source. Using the same irradiation scenario, the $Ta_3B_2@Ta_2O_5$ heterostructures exhibit 80% photocatalytic efficiency. A similar experiment was done on $ZnAl_2O_4/Bi_2MoO_6$ [43] photocatalyst but with a different irradiation scenario (UV light, 100 W), and after 180 min, the MB removal efficiency was 86%. Coupling the photocatalytic process with adsorption represents another way to optimize the energy consumption and to increase the pollutant removal efficiency [44].

This paper presents the correlation between the components mass ratio in a tandem structure and the photocatalytic activity using different radiation scenarios and pollutant molecules. Four tandem structures based on ZnO_SnO_2 and $TiO_2\_SnO_2$ were tested using UV, UV-Vis, and Vis radiations. The tandem structures based on ZnO, TiO_2, and SnO_2 may benefit from the extended light absorption spectra due to the effective band gap established between the components. Additionally, due to their band energies values and efficient charge carrier's separation, the tandem structures are able to exhibits higher performance compare with the individual components [45–47]. The photocatalytic properties were tested using two types of pollutants: pesticide (acetamiprid) and dye (tartrazine). Pesticides and dyes represent two important categories of organic compounds affecting the water properties and consequently the life quality. The water contamination with dyes substances such as tartrazine (Tr) have raised human health issues and this molecule is characterized by strong chemical stability toward traditional wastewater treatment processes due to the aromatic structure [48,49]. The acetamiprid pesticide is considered harmful due to the high toxicity (especially at high concentrations), high accumulation rate, and possible carcinogenic effect induced by their non-biodegradable aromatic structure [50,51]. The results correlate the tandem structure composition with the photocatalytic kinetics based on radiation parameters (wavelength, total irradiance, and photon flux) for each pollutant.

2. Materials and Methods

2.1. Tandem Structures Films Based on Metal Oxides

The ZnO, SnO_2, and TiO_2 metal oxide powders were purchased (Sigma Aldrich, Saint Louis, MO, USA) and used without any purification procedures. Four samples with different mass ratio composition were prepared as follows:

(1) Sample ZnO_SnO_2 (2:1) with a mass ratio between ZnO and SnO_2 of 2:1;
(2) Sample ZnO_SnO_2 (1:2) with a mass ratio between ZnO and SnO_2 of 1:2;
(3) Sample $TiO_2\_SnO_2$ (2:1) with a mass ratio between TiO_2 and SnO_2 of 2:1;
(4) Sample $TiO_2\_SnO_2$ (1:2) with a mass ratio between TiO_2 and SnO_2 of 1:2.

Another three samples containing bare ZnO, SnO_2, and TiO_2 were prepared to be compared with tandem samples.

The deposition technique was a doctor blade and the substrate was microscopic glass. In the first step, the metal oxide-based paste was prepared considering the above mass ration between the components. The metal oxide powder was dispersed into a mixture of ethanol, acetylacetonate, triton ×100 in a volumetric ratio 10:1.5:1.5. The dispersion procedure includes 30 min of vigorous magnetic stirring to assure the paste uniformity. In the second step, the substrate, previously cleaned using surfactants to remove grease traces and then immersed in ethanol for 20 min using an ultrasound bath, was immobilized on a flat surface using a non-conductive transparent tape. The third step is represented by the paste addition (100 µL) on the substrate surface where a glass scraper ensures the uniform paste distribution at constant velocity (1.5 s/cm^2). The last step includes a thermal treatment procedure done at 500 °C for 5 h in order to eliminate the organic additives.

2.2. Photocatalytic Procedures

The photocatalytic experiments where done in a reactor able to assure a uniform light intensity distribution due to 3 light sources placed in suitable positions. The reactor room

is characterized by low humidity and 20–25 °C temperature (depending on the radiation sources). Three light scenarios where employed and the corresponding total irradiance was measured and presented in Table 1. The UV irradiation was provided by 18 W black light Philips tubes T8 model (Amsterdam, Olanda), with 3Lx flux intensity, spectral range between 310 and 390 nm, and a maximum emission at 365 nm. The Vis irradiation was obtained from 18 W white cold light Philips tubes TL-D 80/865 model, with 28Lx flux intensity, spectral range between 400 and 700 nm, and a maximum emission at 565 nm.

Table 1. Irradiation sources and total irradiance.

Irradiation Sources	UV (310–390 nm)	Vis (400–800 nm)	Total Irradiance (W/m^2)	Φ [μmol/(m^2·s)]
UV light	3	0	12.6	24.83
UV-Vis light	2	1	13.8	46.10
Vis light	0	3	17.3	68.42

The irradiance characteristics considering each light source type were E_{UV} = 2.9 W/m^2 corresponding to the UV light and E_{Vis} = 4.2 W/m^2 corresponding to the Vis light. The maximum photon flux, Φ, was calculated using Equation (1) and the values are presented in Table 1. The evaluation takes into consideration the light maximum wavelength ($\lambda_{UV,\,\max}$, $\lambda_{Vis,\,\max}$) as well as the number of irradiation sources (n_{uv} and, respectively, n_{vis}) [52].

$$\Phi = \frac{E_{UV} \cdot \lambda_{UV} \cdot n_{UV} + E_{Vis} \cdot \lambda_{Vis} \cdot n_{Vis}}{h \cdot c \cdot N_{Av}}, \quad (1)$$

where: the Planck constant (h), the speed of light (c), and the Avogadro number have the usual values.

Two organic pollutants were used to evaluate the tandem structures photocatalytic properties: acetamiprid pesticide (Apd) and tartrazine dye (Tr). During the investigation, the tandem structures were immersed for 10 h in 35 mL of pollutant solution (0.025 mM). In the first 120 min, the tandem structures were kept in the dark which is enough to attempt the absorption equilibrium. During the following 8 h, the tandem structures were irradiated based on the three radiation scenarios presented in Table 1. The changes in pollutant concentration were investigated based on the UV-Vis calibration curve and hourly evaluated up to 8 h of photo-catalysis.

The photocatalytic removal efficiency was calculated using Equation (2):

$$\eta = \left[\frac{(C_0 - C)}{C_0}\right] \cdot 100, \quad (2)$$

where: C_0 represents the initial concentration and C represents the pollutant concentration at moment t. The UV-Vis calibration curve based on the absorption spectra of the pollutant was done using the following procedure: (1) several solutions with accurately known concentrations (in the range of working conditions) were prepared; (2) the absorbance at the wavelength of strongest absorption was measured; (3) a graph plot representing the absorbance against concentration was done considering Beer-Lambert law for diluted solutions.

2.3. Investigation Instruments

The crystalline composition was studied using X-ray diffraction (XRD, Bruker D8 Discover Diffractometer, Karlsruhe, Germany) with a setup consisting on locked-couple system at 0.004 degree scan step and 0.02 s/step. Field emission scanning electron microscopy (FE-SEM, SU8010, Fukuoka, Japan) was used to investigate the samples morphology, operated at an accelerated voltage of 25 kV. The optical and photocatalytic investigations were done using the UV-Vis spectrometry (Perkin Elmer Lambda 950, Waltham, MA, USA) technique with a scanning step of 1.0 nm and 6° incidence angle for reflectance measurements. Total

irradiance for each scenario was measured using a class A pyranometer (SR11, Hukselflux, Berlin, Germany) and the sensor was placed in the central position of the sample holder.

3. Results and Discussion

3.1. Composition and Morphology

The diffraction analysis presented in Figure 1 indicates the presence of crystalline structures in all samples, which is a pre-requisite for further photocatalytic applications [53,54]. The peak intensity varies based on the mass ration of each component. There are no additional peaks which may suggest the formation of other non-stoichiometric metal oxides or carbonaceous species [55]. However, possible doping between metal oxides during the post-deposition thermal treatment cannot be excluded. Samples ZnO_SnO_2 contains ZnO with hexagonal crystalline structure (ICCD 89-1397) and SnO_2 with tetragonal structure (ICCD 41-1445) which is consistent with the as-received powders. The ZnO peak intensity increases in sample ZnO_SnO_2 (2:1) where the ZnO ratio is double compared with SnO_2. A similar observation can be done for ZnO_SnO_2 (1:2) where the SnO_2 peak is predominant.

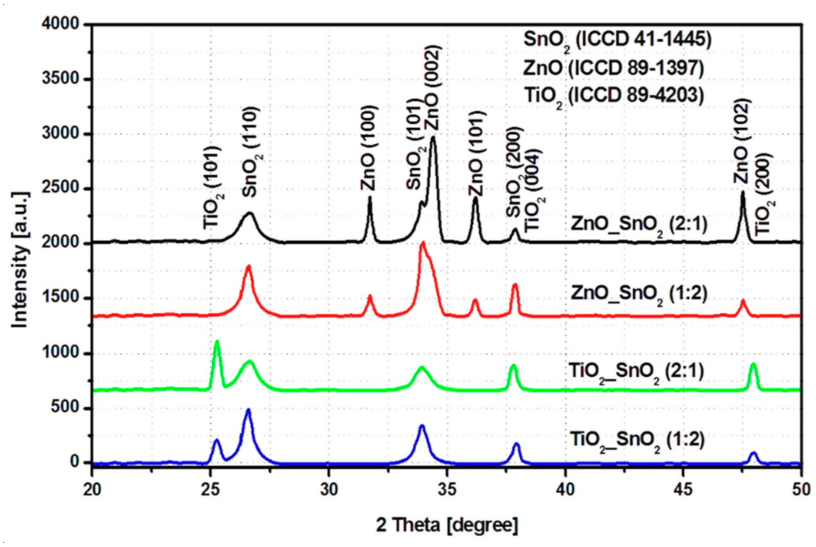

Figure 1. Diffraction patents for the tandem metal oxides structures.

The samples TiO_2_SnO_2 have the characteristic peaks of anatase TiO_2 (ICCD 89-4203) and SnO_2 tetragonal phase. However, there are no peaks corresponding to rutile TiO_2 even if the TiO_2 Degussa contains both crystalline structures. Based on the close proximity of the metal oxide diffraction peaks, the rutile TiO_2 main peak may be covered by the SnO_2 (110) peak intensity which is present in the same diffraction area [56]. The SnO_2 peak intensity increases in sample TiO_2_SnO_2 (1:2) where the SnO_2 ratio is higher. Moreover, the shape of the SnO_2 peaks is different compared with ZnO_SnO_2 samples that may suggest changes of the crystallite sizes [57,58]. The post-deposition thermal treatment used in order to eliminate all the carbonaceous species may also influence the synergy between the metal oxide particles.

The EDS measurements were done to investigate the elemental composition at the tandem structures surface and the results are presented in Table 2. The qualitative results were compared with theoretical oxygen content calculated considering the stoichiometric compounds identified in XRD results. In all samples, the values indicate an oxygen excess which is consistent with our previous studies [59,60] showing that the samples submitted to post-deposition treatment in reach oxygen atmosphere will develop higher oxygen content. The ratio between metal ions at the surface is not the same as the initial values used during the tandem structure deposition. This was expected considering that the deposition method and the dispersive procedure do not allow an accurate control in terms of homogeneity [61]. In this case, the possibility of composition variation may occur especially in bulk where the

tendency of forming aggregates is higher. However, the element which is in higher ratio during the deposition will remain predominant at the sample surface. In addition, due to the annealing treatment in air at elevated temperatures, most of the oxygen vacancies will be passivated according with Equation (3).

$$V_O^- + 1/2O_2 \rightarrow O_O^x + 2h^-. \quad (3)$$

Table 2. Average atomic composition at the surface (EDS) and the corresponding oxygen percentage based on stoichiometric composition.

Components	Elemental Composition [% at]				
	Zn	Ti	Sn	O	O_{th} [1]
ZnO_SnO_2 (2:1)	28.8	-	12.6	56.3	54.0
ZnO_SnO_2 (1:2)	13.8	-	22.5	61.7	58.8
$TiO_2\_SnO_2$ (2:1)	-	19.3	12.1	65.9	62.8
$TiO_2\_SnO_2$ (1:2)	-	10.7	21.3	66.2	64.0

[1] Theoretic content calculated based on the stoichiometry.

The morphology plays an important role in the photocatalytic activity considering that most of the active sites that generate the oxidative species are located on the film surface [62,63]. The results were correlated with the quantitative evaluation of the tandem structures presented in Table 3.

Table 3. Tandem structures quantitative evaluation.

Properties	ZnO	SnO_2	TiO_2	ZnO_SnO_2 (2:1)	ZnO_SnO_2 (1:2)	$TiO_2\_SnO_2$ (2:1)	$TiO_2\_SnO_2$ (1:2)
Thickness [μm] [1]	2.63	2.41	1.88	3.27	3.52	2.13	2.61
Volume [cm^3]	18.07×10^{-5}	17.84×10^{-5}	14.62×10^{-5}	23.68×10^{-5}	28.17×10^{-5}	16.51×10^{-5}	18.33×10^{-5}
Density [g/cm^3]	6.4	6.2	4.9	7.1	6.3	5.4	6.5
Weight [g]	1.15×10^{-3}	1.10×10^{-3}	7.16×10^{-4}	1.68×10^{-3}	1.77×10^{-3}	8.91×10^{-4}	1.19×10^{-3}

[1] Calculated from the reflectance spectra at 6° incident angle.

The SEM images (Figure 2) indicate that the surface morphology depends on the composition ratio of the tandem structure. The mono-component samples (Figure 2a–c) exhibit lower thickness compared to tandem systems due to the uniform particles size (60–80 nm for ZnO, 50–70 nm for SnO_2, and 20–40 nm for TiO_2) used to prepare the precursor paste. The aggregates formation is present in all samples but the size is lower in mono-component samples compared with the tandem system. The tandem systems include particles with various sizes which have the tendency to form larger agglomerations which are not completely dispersed during the diffusion process. Sample ZnO_SnO_2 (2:1) (Figure 2d) exhibits higher density compared with sample ZnO_SnO_2 (1:2) and large grains with irregular shape. When SnO_2 is the majority component, the sample density increases as well as the film thickness. Sample ZnO_SnO_2 (1:2) shows a porous morphology and a thickness of around 3.52 μm. However, the tandem sample composed from TiO_2 and SnO_2 presents small grains closely packed and smaller thickness values which indicate a good structural compatibility between the components. The formation of surface irregularities on the $TiO_2\_SnO_2$ samples may be attributed to the residual particles that occur during the post-deposition thermal treatment [64,65]. The extension of these irregularities is limited, indicating that it is not a characteristic of the tandem structures morphology. The organic additives were used to increase the mechanical adhesion on the microscopic glass substrate, otherwise there is a risk of film collapse during the photocatalytic experiments [66].

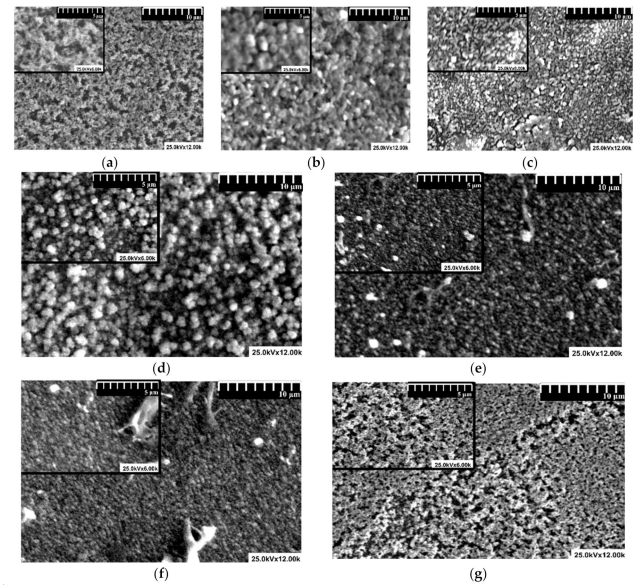

Figure 2. Scanning electron microscopy images of the samples: (**a**) ZnO, (**b**) SnO_2, (**c**) TiO_2, (**d**) ZnO_SnO_2 (2:1), (**e**) ZnO_SnO_2 (1:2), (**f**) TiO_2_SnO_2 (2:1), and (**g**) TiO_2_SnO_2 (1:2).

3.2. Photocatalytic Activity

3.2.1. Photocatalytic Efficiencies and Kinetics

The photocatalytic removal efficiency of Tr and Apd molecules were tested for all tandem structures using three different irradiation scenarios. The lowest photocatalytic efficiencies (Figure 3a,b) were obtained using a Vis irradiation scenario due to the metals oxides band gap energies which correspond to the UV region.

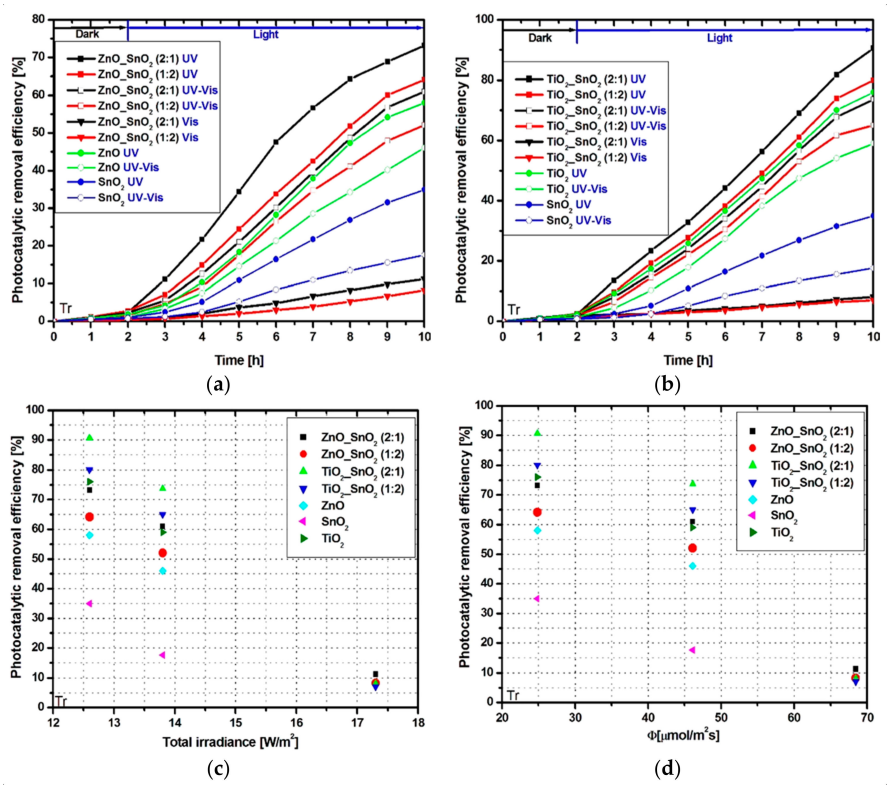

Figure 3. Photocatalytic activity toward Tr molecule: (**a**,**b**) removal efficiency, (**c**) photocatalytic removal efficiency vs. total irradiance, and (**d**) photocatalytic removal efficiency vs. photon flux.

The bare ZnO and TiO_2 samples exhibit 58% and, respectively, 76% photocatalytic removal efficiencies under UV irradiation. The lowest photocatalytic activity was recorded for bare SnO_2 which is able to reach only 35% efficiency using UV light sources. The tandem structures show higher photocatalytic activity due to the cumulated effect of multiple charge carriers generation and low recombination rate. The highest efficiency of 90% was recorded for Tr removal during the UV irradiation of TiO_2_SnO_2 (2:1) sample (Figure 3b). Using the same irradiation scenario but changing the TiO_2_SnO_2 ratio to 1:2, the photocatalytic removal efficiency decreased to 80%. These results indicate that TiO_2 content in the TiO_2_SnO_2 tandem structure is the driving photocatalitic factor with a significant contribution on the pollutant removal efficiency.

The ZnO_SnO_2 samples exhibit similar photocatalytic behavior (Figure 3a) and reach 73% photocatalytic efficiency under UV irradiation when the ZnO_SnO_2 ratio is 2:1. The total irradiance (Figure 3c) and the photon flux (Figure 3d) evaluations indicate that in order to obtain high photocatalytic values the wavelength radiation must be correlated with the photocatalytic materials. Otherwise, high irradiance and photon flux is not enough to enhance the photocatalytic properties. By coupling UV with Vis radiation, the photocatalytic removal efficiency decreases due to the lower photons concentration available to generate the oxidative species during the Tr removal.

The Apd photocatalytic removal efficiency (Figure 4a,b) is lower compared with Tr due to the higher chemical stability of the Apd molecule [67].

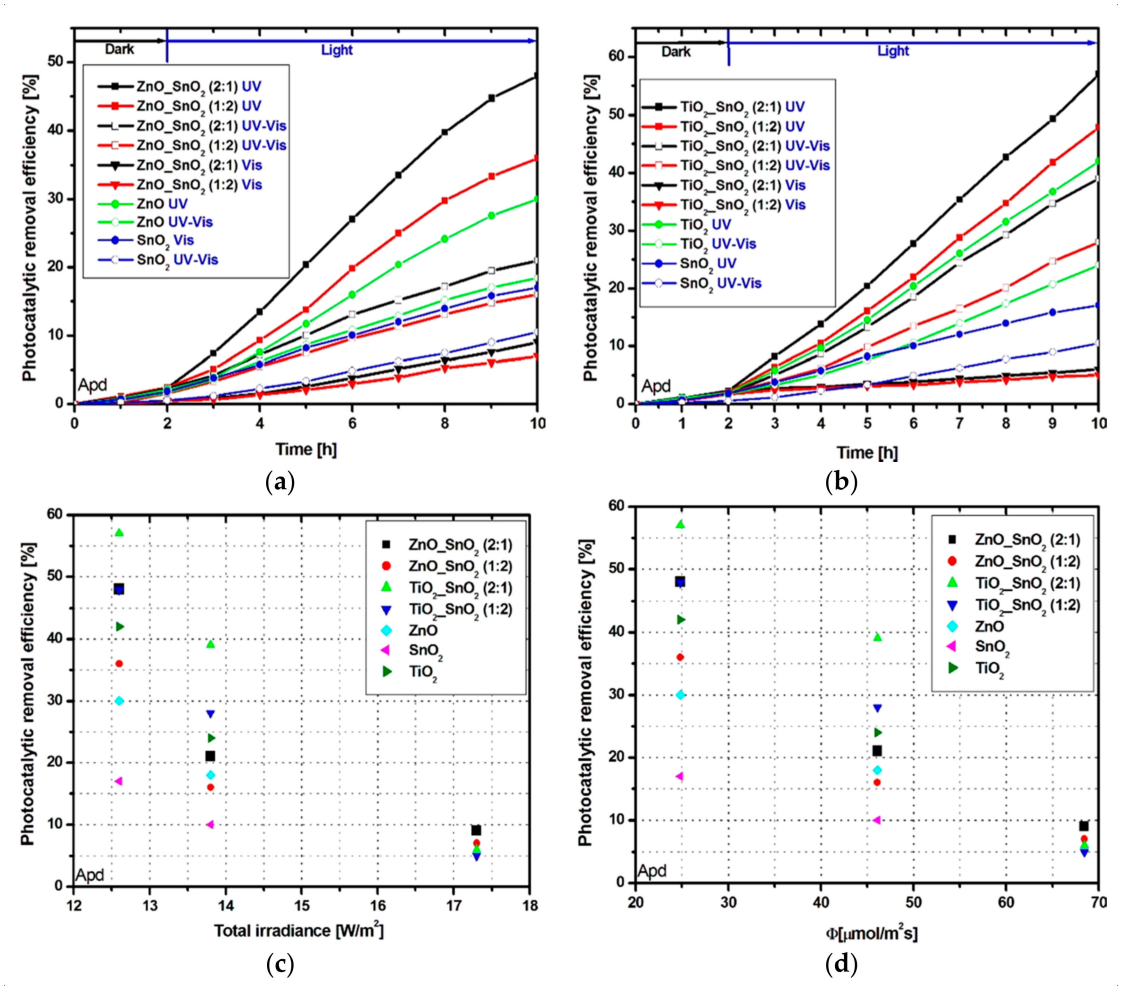

Figure 4. Photocatalytic activity toward Apd molecule: (**a**,**b**) removal efficiency, (**c**) total irradiance vs. pollutant removal efficiency, and (**d**) photocatalytic removal efficiency vs. photon flux.

The highest photocatalytic efficiency (Figure 4b) was recorded for sample TiO_2_SnO_2 (2:1) under UV irradiation able to reach 57% compared with 42% for bare TiO_2 or 30% for bare ZnO. However, the difference between TiO_2_SnO_2 and ZnO_SnO_2 samples in terms of photocatalytic activity is not so obvious for the Apd molecule. Due to the higher induction period, the samples require a longer period to produce enough oxidative species (manly $^{\cdot}O_2^-$, HO^- radicals) necessary to decompose the pollutant molecules. Figure 4c,d indicates that using 12.6 W/cm^2 total irradiance and 24.83 µmol/m^2·s photo flux from UV sources can induce an increase of the photocatalytic activity compared with 17.3 W/cm^2 and 68.42 µmol/m^2·s from Vis sources. Based on the photocatalytic efficiency curve shape, the ZnO_SnO_2 samples will reach the saturation point faster compared with TiO_2_SnO_2 tandem structures. In this case, longer irradiation periods can increase the photocatalytic activities differences between the samples.

Furthermore, the influence of the light radiation and tandem structure composition was correlated with the photocatalytic kinetic data, based on the simplified Langmuir-Hinshelwood (L-H) mathematical equation, see Equation (4):

$$\ln C/C_0 = -kt. \quad (4)$$

The kinetic evaluation of the Tr photocatalytic removal (Figure 5) indicates that the rate constant is almost double (Table 4) when TiO_2/SnO_2 samples are irradiated with UV radiation compared with mixed UV-Vis radiation. Additionally, the photocatalytic activity under UV radiation of the TiO_2_SnO_2 samples is 28× faster compared with Vis radiation.

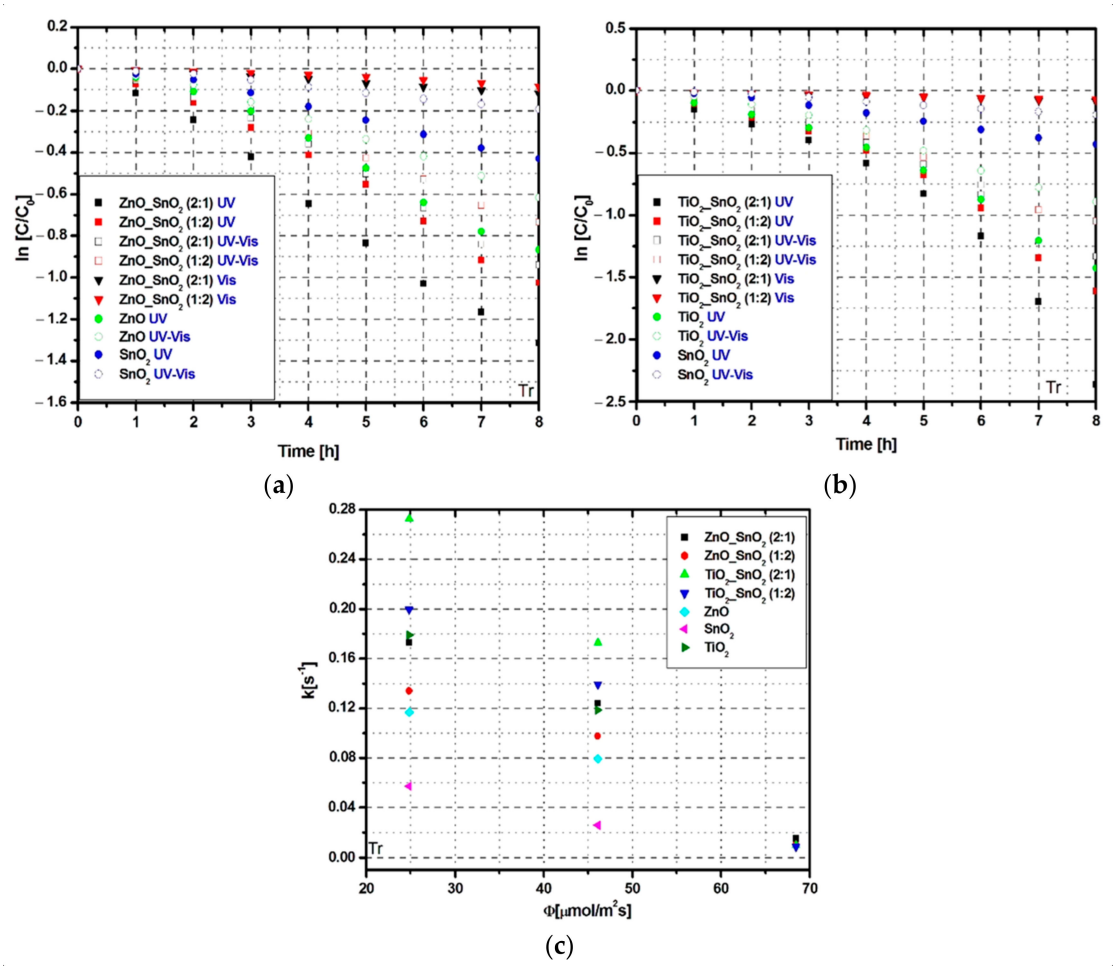

Figure 5. Kinetic evaluation of photocatalytic activity toward Tr molecule: (**a**,**b**) removal kinetics, (**c**) photon flux vs. removal rate constant.

Table 4. Kinetic data corresponding to Tr pollutant.

Kinetic Data	ZnO_SnO_2 (2:1)		ZnO_SnO_2 (1:2)		$TiO_2\_SnO_2$ (2:1)		$TiO_2\_SnO_2$ (1:2)		ZnO		SnO_2		TiO_2	
	k [s^{-1}]	R^2	k [s^{-1}]	R^2	k [s^{-1}]	R^2	k [s^{-1}]	R^2	k [s^{-1}]	R^2	k [s^{-1}]	R^2	k [s^{-1}]	R^2
Tr														
UV	0.1731	0.9972	0.1340	0.9922	0.2724	0.9495	0.1997	0.9709	0.1169	0.9885	0.0571	0.9927	0.1790	0.9771
UV-Vis	0.1240	0.9898	0.0976	0.9927	0.1728	0.9724	0.1392	0.9842	0.0794	0.0016	0.0257	0.9940	0.1187	0.9870
Vis	0.0153	0.9962	0.0104	0.9840	0.0097	0.9910	0.0086	0.9938	-	-	-	-	-	-
Adp														
UV	0.0844	0.9987	0.0582	0.9979	0.1030	0.9910	0.0804	0.9904	0.0462	0.9989	0.0228	0.9959	0.0678	0.9950
UV-Vis	0.0291	0.9954	0.0214	0.9962	0.0624	0.9949	0.0406	0.9954	0.0252	0.9968	0.0139	0.9977	0.0340	0.9938
Vis	0.0199	0.9942	0.0092	0.9943	0.0063	0.9456	0.0063	0.9456	-	-	-	-	-	-

Lower differences are recorded for ZnO_SnO_2 samples where the photocatalytic activity under UV radiation is 1.4× higher compared with mixed UV–Vis radiation and 11× faster compared with Vis radiation. Based on the comparative evaluation of the rate constant vs. photon flux (Figure 5c), $TiO_2\_SnO_2$ (2:1) exhibits the optimum photocatalytic activity for both UV and UV-Vis radiation scenarios.

The kinetic evaluation for Apd photocatalytic removal (Figure 6) indicates that the reaction rate decreases significantly compared with Tr photocatalytic removal and the differences between radiation scenarios are lower.

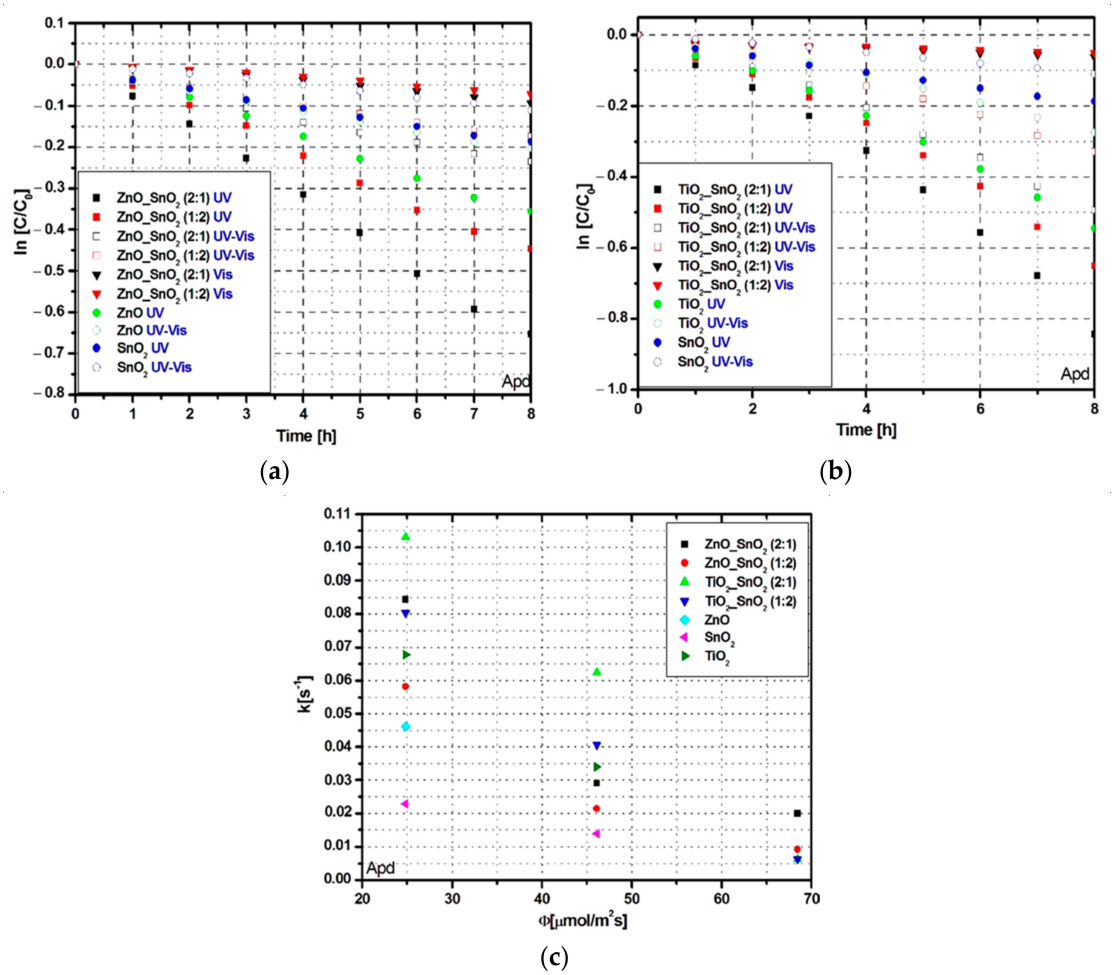

Figure 6. Kinetic evaluation of photocatalytic activity toward Apd molecule: (**a**,**b**) removal kinetics, (**c**) photon flux vs. removal rate constant.

Even if the photocatalytic activity remains higher under UV radiation, the reaction rate is influenced by the pollutant molecule stability. The TiO_2_SnO_2 and ZnO_SnO_2 samples exhibit under UV radiation 2× higher photocatalytic activity compared with UV-Vis radiation. However, this results indicate that the ZnO_SnO_2 (2:1) sample is suitable for the pesticide removal and the rate constant (Figure 6c) at 24.83 µmol/m^2·s photo flux is higher comparative with the TiO_2_SnO_2 (1:2) tandem structure.

The influence of photon absorption based on the UV scenario was evaluated using the L-H model proposed by Turchi and Ollis [68]:

$$r = -\frac{dC}{dt} = \frac{k_r K_S C}{1 + K_S C}, \quad (5)$$

where k_r (mol/L·min) represent the apparent reaction rate constant, C is the acetamiprid and tartrazine (Tr and Apd) concentrations (mol/L), r (mol/L·min) represent the photocatalytic removal rate, and K_S (L/mol) is the apparent adsorption constant. Consequently, the $k_r \cdot K_S$ term is used to describe the apparent rate constant k (min^{-1}) corresponding to the photocatalytic activity. The k_r constant should consider the photon flux values and Equation (5) can be changed accordingly:

$$\frac{1}{r} = \frac{1}{k_r K_S} \cdot \frac{1}{C} + \frac{1}{k_r}. \quad (6)$$

Using the linear plot $1/C$ vs. $1/r$, as well as the $(1/k_r)$ intercept and the $(/k_r K_S)$ slope allow evaluating the kinetic parameters, and the results obtained for UV radiation are presented in Table 5.

Table 5. Kinetic parameters based on Equation (6) for UV radiation.

Tandem Structure, Pollutant	$k_r \cdot 10^8$ (mol/L·min)	K_S (mol/L)
ZnO/SnO_2 (2:1), Tr	4.13	163,392.4
ZnO/SnO_2 (2:1), Apd	2.44	105,831.8
ZnO/SnO_2 (1:2), Tr	1.83	95,273.5
ZnO/SnO_2 (1:2), Apd	1.38	48,527.9
TiO_2/SnO_2 (2:1), Tr	5.28	294,772.3
TiO_2/SnO_2 (2:1), Apd	3.71	149,934.0
TiO_2/SnO_2 (1:2), Tr	5.14	263,972.6
TiO_2/SnO_2 (1:2), Apd	3.53	135,729.1

The values based on the mathematical model indicate that L-H exhibit a good fit with the experimental data for ZnO_SnO_2 (2:1), TiO_2_SnO_2 (2:1), and TiO_2_SnO_2 (1:2) tandem structures. In these three situations, the apparent reaction rates and the apparent adsorption constant have the some order of magnitude, while for the ZnO_SnO_2 (1:2) tandem structure, there is one order of magnitude difference. These results were also observed by Isac et al. [69], showing that using tandem structures based on metal oxides with compatible band gaps will favor the charge carriers photogeneration and conversion to oxidative species. The results show that it is feasible to consider that the degradation mechanism is affected not only by the radiation type but also by the pollutant chemical stability during the photocatalytic activity.

3.2.2. Photocatalytic Mechanisms

The structure representation of the tandem components band energies (Figure 7) will provide additional information regarding the photocatalytic experimental results. The charge carriers concentration and mobility depend on the suitable disposal of the energy bands and were evaluated based on the Gao et al. [70] and Mise et al. [71] algorithms. The details procedure for the conduction band (CB) and valence band (VB) potentials evaluation for tandem structure was previously presented [72].

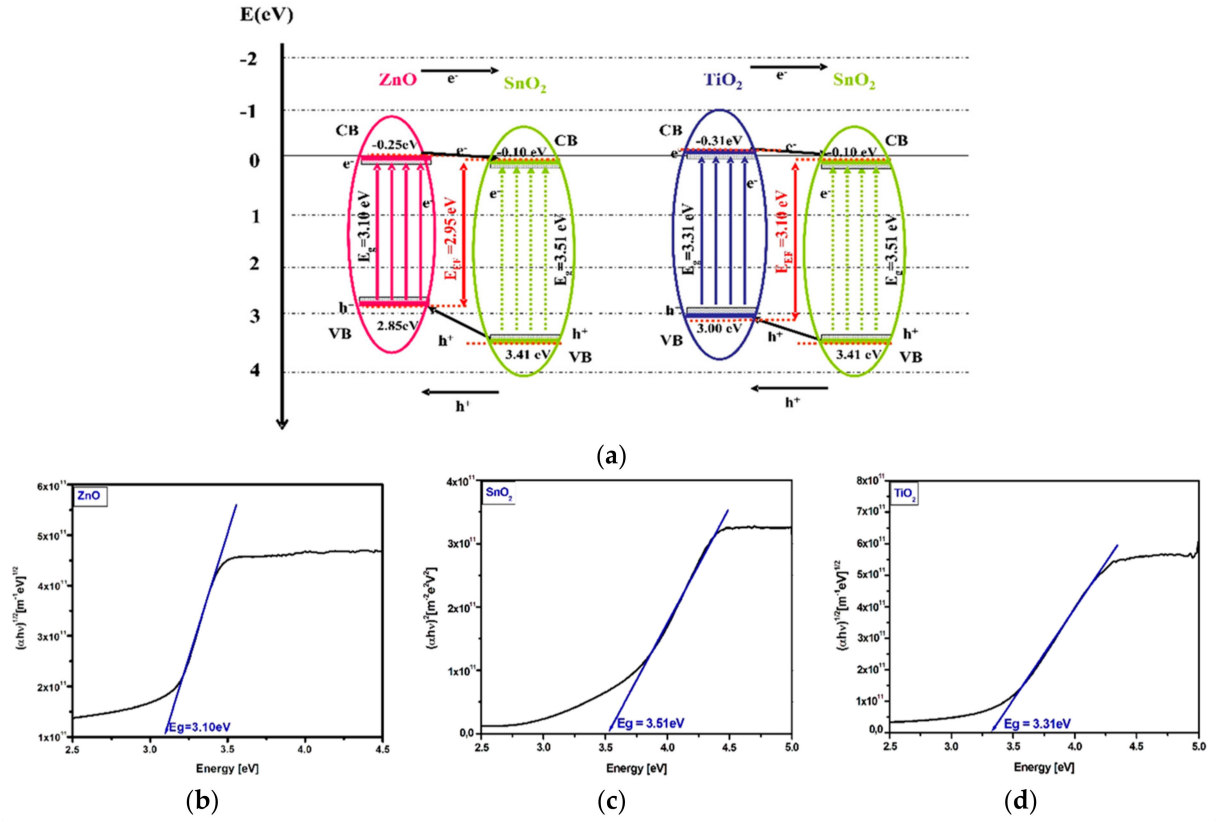

Figure 7. Band energy diagrams (**a**) and the corresponding band gap values (**b**–**d**).

The bands energy diagram indicates that under light irradiation the photogenerated electrons from the SnO_2 valence band are transferred on zinc oxide valence band which is the closest energy level in the ZnO_SnO_2 tandem structure or on titanium oxide valence band in the TiO_2_SnO_2 sample. The photogenerated electron-hole pairs within the charged space region are efficiently separated by the electric field [73]. The charge carrier's insertion in the depletion layer will induce an increase of the concentration gradient over the tandem structure, resulting in the development of a diffuse layer [74,75]. Consequently, due to the combined effect of drift and diffusion, the photogenerated electrons and holes will flow through the tandem components. The ZnO, TiO_2, and SnO_2 conduction band (CB) edges are situated at −0.25, −0.31, and −0.10 eV vs. normal hydrogen electrode (NHE). The SnO_2 valence band (VB) edge (+3.41 eV) is lower compared to ZnO (+2.85 eV) and TiO_2 (+3.00 eV). The charge carrier's diffusion in both tandem structures will evolve form the SnO_2 valence band to the most closely energy level represented by the ZnO or TiO_2 valence band and overcome the band gap energy in order to transfer in the conduction bands [76]. The effective band gap value of the ZnO_SnO_2 and TiO_2_SnO_2 tandem systems was evaluated according to Scanlon et al. [77]. The results confirm the extended Vis activation (up to 420 nm) of the ZnO_SnO_2 which explain the presence of photocatalytic activity (even at low values) under the Vis irradiation. As expected, there is no evidence that the band gap values depends on the mass ration between the components.

The pollutant mineralization is related with the tandem structure ability to generate interfacial oxidative species according to the following Equations (7)–(10):

$$\text{Tandem structure} + h\nu \rightarrow e^- + h^+, \quad (7)$$

$$h^+ \text{ (Tandem structure)} + H_2O \rightarrow OH \text{ (Tandem structure)} + H^+, \quad (8)$$

$$\text{Organic Pollutant} + OH \rightarrow \text{Photocatalysis products}, \quad (9)$$

$$O_2 + e^- \rightarrow O_2^- \text{ (aqueous solution)}. \quad (10)$$

4. Conclusions

The photocatalytic activity evaluation shows that the highest efficiency (90%) for Tr dye removal was obtained for sample TiO_2_SnO_2 (2:1) under UV radiation. Based on the same radiation scenario, the ZnO_SnO_2 (2:1) sample exhibits 70% photocatalytic removal efficiency. The photocatalytic reaction rate is significantly influenced by the radiation type and tandem composition. The TiO_2_SnO_2 samples reaction rate is double under UV radiation compared with UV–Vis radiation and 28× higher compared with Vis radiation. Compared with bare ZnO, SnO_2, and TiO_2, the tandem structures exhibit improved photocatalytic efficiency due to the lower recombination rate and higher photogenerated charge carrier density.

The changes in the photocatalytic activity are smaller during the Apd photocatalytic removal. The reaction rate for TiO_2_SnO_2 samples is 13× higher in UV compared with Vis radiation. Additionally, the constant rate of the ZnO_SnO_2 (2:1) sample is higher than that of TiO_2_SnO_2 (1:2) under UV radiation. The charge carriers mobility based on the energy band diagram indicate that the photogenerated electrons follows the type II mechanism and have a significant contribution on the development of oxidative species.

These results indicate that the photocatalytic process optimization should consider a suitable optimization between the radiation sources, photon flux, catalyst materials, and pollutant type. Using high irradiance and photon flux is not enough to assure high photocatalytic efficiency. The correlations of the irradiation scenario with photocatalyst materials and pollutant type will have a positive impact on the overall photocatalytic efficiency, improving the charge carrier's photogeneration and the formation of oxidative species.

Author Contributions: Conceptualization, A.E.; methodology, A.E.; software, L.I.; validation, A.E. and L.I.; formal analysis, L.I.; investigation, L.I.; resources, A.E.; data curation, L.I.; writing—original draft preparation, A.E.; writing—review and editing, A.E.; visualization, L.I.; supervision, A.E.; project administration, A.E.; funding acquisition, A.E. All authors have read and agreed to the published version of the manuscript.

Funding: This work was supported by a grant of the Romanian Ministry of Education and Research, CCCDI-UEFISCDI, project number PN-III-P2-2.1-PED-2019-2028, within PNCDI III.

Data Availability Statement: Data presented in this study are available by requesting from the corresponding author.

Acknowledgments: The authors would like to acknowledge the Tokyo University of Science for their support on the experimental investigations.

Conflicts of Interest: The authors declare no conflict of interest.

References

1. Milenković, D.A.; Dimić, D.S.; Marković, Z.S. Advanced oxidation process of coumarins by hydroxyl radical: Towards the new mechanism leading to less toxic products. *Chem. Eng. J.* **2020**, *395*, 124971. [CrossRef]
2. Na, S.; Seo, S.; Lee, H. Recent developments of advanced Ti^{3+}-self-doped TiO_2 for efficient visible-light-driven photocatalysis. *Catalysts* **2020**, *10*, 679. [CrossRef]
3. Al-Kandari, H.; Younes, N.; Al-Jamal, O.; Zakaria, Z.Z.; Najjar, H.; Alserr, F.; Pintus, G.; Al-Asmakh, M.; Abdullah, A.M.; Nasrallah, G.K. Ecotoxicological assessment of thermally- and hydrogen-reduced graphene oxide/TiO_2 photocatalytic nanocomposites using the zebrafish embryo model. *Nanomaterials* **2019**, *9*, 488. [CrossRef] [PubMed]
4. Yu, S.; Han, B.; Lou, Y.; Liu, Z.; Qian, G.; Wang, Z. Rational design and fabrication of TiO_2 nano heterostructure with multi-junctions for efficient photocatalysis. *Int. J. Hydrog. Energy* **2020**, *45*, 28640–28650. [CrossRef]
5. Li, L.; Zheng, X.; Chi, Y.; Wang, Y.; Sun, X.; Yue, Q.; Gao, B.; Xu, S. Molecularly imprinted carbon nanosheets supported TiO_2: Strong selectivity and synergic adsorption-photocatalysis for antibiotics removal. *J. Hazard. Mater.* **2020**, *383*, 121211. [CrossRef]
6. Periyasamy, M.; Saha, A.; Sain, S.; Mandal, M.; Sengupta, U.; Kar, A. A comparative structural and photocatalytic study on SnO_2 nanoparticles fabricated in batch reactor and microreactor. *J. Environ. Chem. Eng.* **2020**, *8*, 104604. [CrossRef]
7. Enesca, A.; Duta, A. The influence of organic additives on the morphologic and crystalline properties of SnO2 obtained by spray pyrolysis deposition. *Thin Solid Films* **2011**, *519*, 5780–5786. [CrossRef]
8. Cai, X.; Huang, Y.; Hu, J.; Zhu, S.; Tian, X.; Zhang, K.; Ji, G.; Zhang, Y.; Fu, Z.; Tan, C. Tuning photocatalytic performance of multilayer ZnO for water splitting by biaxial strain composites. *Catalysts* **2020**, *10*, 1208. [CrossRef]

9. Hernández-Carrillo, M.; Torres-Ricárdez, R.; García-Mendoza, M.; Ramírez-Morales, E.; Rojas-Blanco, L.; Díaz-Flores, L.; Sepúlveda-Palacios, G.; Paraguay-Delgado, F.; Pérez-Hernández, G. Eu-modified ZnO nanoparticles for applications in photocatalysis. *Catal. Today* **2020**, *349*, 191–197. [CrossRef]
10. Li, J.; Zhao, Y.; Xia, M.; An, H.; Bai, H.; Wei, J.; Yang, B.; Yang, G. Highly efficient charge transfer at 2D/2D layered P-$La_2Ti_2O_7$/Bi_2WO_6 contact heterojunctions for upgraded visible-light-driven photocatalysis. *Appl. Catal. B Environ.* **2020**, *261*, 118244. [CrossRef]
11. Gao, X.; Niu, J.; Wang, Y.; Ji, Y.; Zhang, Y. Solar photocatalytic abatement of tetracycline over phosphate oxoanion decorated Bi_2WO_6/polyimide composites. *J. Hazard. Mater.* **2021**, *403*, 123860. [CrossRef] [PubMed]
12. Li, X.Z.; Wu, K.L.; Dong, C.; Xia, S.H.; Ye, Y.; Wei, X. Size-controlled synthesis of Ag_3PO_4 nanorods and their high-performance photocatalysis for dye degradation under visible-light irradiation. *Mater. Lett.* **2014**, *130*, 97–100. [CrossRef]
13. Nyankson, E.; Kumar, R. Removal of water-soluble dyes and pharmaceutical wastes by combining the photocatalytic properties of Ag_3PO_4 with the adsorption properties of halloysite nanotubes. *Mater. Today Adv.* **2019**, *4*, 100025. [CrossRef]
14. Naciri, Y.; Hsini, A.; Ajmal, Z.; Navío, J.A.; Bakiz, B.; Albourine, A.; Ezahri, M.; Benlhachemi, A. Recent progress on the enhancement of photocatalytic properties of $BiPO_4$ using π–conjugated materials. *Adv. Colloid Interface Sci.* **2020**, *280*, 102160. [CrossRef] [PubMed]
15. Koutavarapu, R.; Tamtam, M.R.; Rao, M.C.; Cho, M.; Shim, J. Enhanced solar-light-driven photocatalytic properties of novel Z-scheme binary $BiPO_4$ nanorods anchored onto $NiFe_2O_4$ nanoplates: Efficient removal of toxic organic pollutants. *J. Environ. Sci.* **2021**, *102*, 326–340. [CrossRef]
16. Todorova, N.; Papailias, I.; Giannakopoulou, T.; Ioannidis, N.; Boukos, N.; Dallas, P.; Edelmannová, M.; Reli, M.; Kočí, K.; Trapalis, C. Photocatalytic H_2 evolution, CO_2 reduction, and NO_x oxidation by highly exfoliated g-C_3N_4. *Catalysts* **2020**, *10*, 1147. [CrossRef]
17. Ismael, M. A review on graphitic carbon nitride (g-C_3N_4) based nanocomposites: Synthesis, categories, and their application in photocatalysis. *J. Alloy. Compd.* **2020**, *846*, 156446. [CrossRef]
18. Desseigne, M.; Dirany, N.; Chevallier, V.; Arab, M. Shape dependence of photosensitive properties of WO_3 oxide for photocatalysis under solar light irradiation. *Appl. Surf. Sci.* **2019**, *483*, 313–323. [CrossRef]
19. Xu, X.; Liu, S.; Cui, Y.; Wang, X.; Smith, K.; Wang, Y. Solar-driven removal of 1,4-dioxane using WO_3/nγ-Al_2O_3 nano-catalyst in water. *Catalysts* **2019**, *9*, 389. [CrossRef]
20. Yadav, M.; Garg, S.; Chandra, A.; Hernadi, K. Immobilization of green BiOX (X = Cl, Br and I) photocatalysts on ceramic fibers for enhanced photocatalytic degradation of recalcitrant organic pollutants and efficient regeneration process. *Ceram. Int.* **2019**, *45*, 17715–17722. [CrossRef]
21. Gao, B.; Zhang, J.-R.; Chen, L.; Guo, J.; Shen, S.; Au, C.T.; Yin, S.F.; Cai, M.Q. Density functional theory calculation on two-dimensional MoS_2/BiOX (X = Cl, Br, I) van der Waals heterostructures for photocatalytic action. *Appl. Surf. Sci.* **2019**, *492*, 157–165. [CrossRef]
22. Kumari, P.; Bahadur, N.; O'Dell, L.A.; Kong, L.; Sadek, A.; Merenda, A.; Dumée, L.F. Nanoscale 2D semi-conductors—Impact of structural properties on light propagation depth and photocatalytic performance. *Sep. Purif. Technol.* **2021**, *258*, 118011. [CrossRef]
23. Wu, J.; Wang, W.; Tian, Y.; Song, C.; Qiu, H.; Xue, H. Piezotronic effect boosted photocatalytic performance of heterostructured $BaTiO_3$/TiO_2 nanofibers for degradation of organic pollutants. *Nano Energy* **2020**, *77*, 105122. [CrossRef]
24. Xue, J.; Lei, D.; Bi, Q.; Tang, C.; Zhang, L. Enhancing photocatalytic performance of Zn_2SnO_4 by doping Yb: Oxygen vacancies formation and dye self-sensitization degradation. *Opt. Mater.* **2020**, *108*, 110454. [CrossRef]
25. Huang, S.; Zhang, J.; Qin, Y.; Song, F.; Du, C.; Su, Y. Direct Z-scheme SnO_2/$Bi_2Sn_2O_7$ photocatalyst for antibiotics removal: Insight on the enhanced photocatalytic performance and promoted charge separation mechanism. *J. Photochem. Photobiol. A Chem.* **2021**, *404*, 112947. [CrossRef]
26. Lin, Y.; Pan, D.; Luo, H. Hollow direct Z-Scheme CdS/$BiVO_4$ composite with boosted photocatalytic performance for RhB degradation and hydrogen production. *Mater. Sci. Semicond. Process.* **2021**, *121*, 105453. [CrossRef]
27. Chen, C.; Liu, X.; Fang, Q.; Chen, X.; Liu, T.; Zhang, M. Self-assembly synthesis of CuO/ZnO hollow microspheres and their photocatalytic performance under natural sunlight. *Vacuum* **2020**, *174*, 109198. [CrossRef]
28. Krawczyk, K.; Wacławek, S.; Kudlek, E.; Silvestri, D.; Kukulski, T.; Grübel, K.; Padil, V.V.; Cernik, M. UV-catalyzed persulfate oxidation of an anthraquinone based dye. *Catalysts* **2020**, *10*, 456. [CrossRef]
29. Bansal, P.; Verma, A.; Talwar, S. Detoxification of real pharmaceutical wastewater by integrating photocatalysis and photo-Fenton in fixed-mode. *Chem. Eng. J.* **2018**, *349*, 838–848. [CrossRef]
30. Bonora, R.; Boaretti, C.; Campea, L.; Roso, M.; Martucci, A.; Modesti, M.; Lorenzetti, A. Combined AOPs for formaldehyde degradation using heterogeneous nanostructured catalysts. *Nanomaterials* **2020**, *10*, 148. [CrossRef]
31. Khan, S.H.; Pathak, B. Zinc oxide based photocatalytic degradation of persistent pesticides: A comprehensive review. *Environ. Nanotechnol. Monit. Manag.* **2020**, *13*, 100290. [CrossRef]
32. Mouchaal, Y.; Enesca, A.; Mihoreanu, C.; Khelil, A.; Duta, A. Tuning the opto-electrical properties of SnO_2 thin films by Ag^{+1} and In^{+3} co-doping. *Mater. Sci. Eng. B* **2015**, *199*, 22–29. [CrossRef]
33. Kaplan, A.; Mamane, H.; Lester, Y.; Avisar, D. Trace organic compound removal from wastewater reverse-osmosis concentrate by advanced oxidation processes with UV/O_3/H_2O_2. *Materials* **2020**, *13*, 2785. [CrossRef] [PubMed]

34. Yang, X.; Koziel, J.A.; Laor, Y.; Zhu, W.; van Leeuwen, J.H.; Jenks, W.S.; Hoff, S.J.; Zimmerman, J.; Zhang, S.; Ravid, U.; et al. VOC removal from manure gaseous emissions with UV photolysis and UV-TiO_2 photocatalysis. *Catalysts* **2020**, *10*, 607. [CrossRef]
35. He, X.; Wu, M.; Ao, Z.; Lai, B.; Zhou, Y.; An, T.; Wang, S. Metal-organic frameworks derived C/TiO_2 for visible light photocatalysis: Simple synthesis and contribution of carbon species. *J. Hazard. Mater.* **2021**, *403*, 124048. [CrossRef] [PubMed]
36. Saoud, W.A.; Assadi, A.A.; Guiza, M.; Bouzaza, A.; Aboussaoud, W.; Ouederni, A.; Soutrel, I.; Wolbert, D.; Rtimi, S. Study of synergetic effect, catalytic poisoning and regeneration using dielectric barrier discharge and photocatalysis in a continuous reactor: Abatement of pollutants in air mixture system. *Appl. Catal. B Environ.* **2017**, *213*, 53–61. [CrossRef]
37. Franz, S.; Falletta, E.; Arab, H.; Murgolo, S.; Bestetti, M.; Mascolo, G. Degradation of carbamazepine by photo(electro)catalysis on nanostructured TiO_2 meshes: Transformation products and reaction pathways. *Catalysts* **2020**, *10*, 169. [CrossRef]
38. Mohan, S.; Mamane, H.; Avisar, D.; Gozlan, I.; Kaplan, A.; Dayalan, G. Treatment of diethyl phthalate leached from plastic products in municipal solid waste using an ozone-based advanced oxidation process. *Materials* **2019**, *12*, 4119. [CrossRef] [PubMed]
39. De Richter, R.; Ming, T.; Davies, P.L.; Liu, W.; Caillol, S. Removal of non-CO_2 greenhouse gases by large-scale atmospheric solar photocatalysis. *Prog. Energy Combust. Sci.* **2017**, *60*, 68–96. [CrossRef]
40. Ojha, D.P.; Song, J.H.; Kim, H.J. Facile synthesis of graphitic carbon-nitride supported antimony-doped tin oxide nanocomposite and its application for the adsorption of volatile organic compounds. *J. Environ. Sci.* **2019**, *79*, 35–42. [CrossRef]
41. Zhao, K.; Zhang, Z.; Feng, Y.; Lin, S.; Li, H.; Gao, X. Surface oxygen vacancy modified Bi_2MoO_6/MIL-88B(Fe) heterostructure with enhanced spatial charge separation at the bulk & interface. *Appl. Catal. B Environ.* **2020**, *268*, 118740. [CrossRef]
42. Li-Hong, B.; Yang, F.; Cheng, D.; Pan, X.; Zhang, H.; Zhao, F.; Zhao, S.; Tegus, O. Modified electronic structure of Ta_2O_5 via surface decorated with Ta_3B_2 nanodots for enhanced photocatalytic activity. *Appl. Surf. Sci.* **2020**, *513*, 145767. [CrossRef]
43. Tian, Q.; Fang, G.; Ding, L.; Ran, M.; Zhang, H.; Pan, A.; Shen, K.; Deng, Y. $ZnAl_2O_4$/Bi_2MoO_6 heterostructures with enhanced photocatalytic activity for the treatment of organic pollutants and eucalyptus chemimechanical pulp wastewater. *Mater. Chem. Phys.* **2020**, *241*, 122299. [CrossRef]
44. Giovannetti, R.; Rommozzi, E.; D'Amato, C.A.; Zannotti, M. Kinetic model for simultaneous adsorption/photodegradation process of alizarin red S in water solution by nano-TiO_2 under visible light. *Catalysts* **2016**, *6*, 84. [CrossRef]
45. Losch, P.; Huang, W.; Goodman, E.D.; Wrasman, C.J.; Holm, A.; Riscoe, A.R.; Schwalbe, J.A.; Cargnello, M. Colloidal nanocrystals for heterogeneous catalysis. *Nano Today* **2019**, *24*, 15–47. [CrossRef]
46. Pirhashemi, M.; Habibi-Yangjeh, A. Photosensitization of ZnO by AgBr and Ag_2CO_3: Nanocomposites with tandem n-n heterojunctions and highly enhanced visible-light photocatalytic activity. *J. Colloid Interface Sci.* **2016**, *474*, 103–113. [CrossRef] [PubMed]
47. Durán-Álvarez, J.C.; Avella, E.; Ramírez-Zamora, R.M.; Zanella, R. Photocatalytic degradation of ciprofloxacin using mono- (Au, Ag and Cu) and bi- (Au–Ag and Au–Cu) metallic nanoparticles supported on TiO_2 under UV-C and simulated sunlight. *Catal. Today* **2016**, *266*, 175–187. [CrossRef]
48. Libralato, G.; Lofrano, G.; Siciliano, A.; Gambino, E.; Boccia, G.; Federica, C.; Francesco, A.; Galdiero, E.; Gesuele, R.; Guida, M. Toxicity assessment of wastewater after advanced oxidation processes for emerging contaminants' degradation. In *Visible Light Active Structured Photocatalysts for the Removal of Emerging Contaminants*, 1st ed.; Sacco, O., Vaiano, V., Eds.; Elsevier: New York, NY, USA, 2020; pp. 195–211.
49. Berberidou, C.; Kitsiou, V.; Poulios, I. Evaluation of an alternative method for wastewater treatment containing pesticides using solar photocatalytic oxidation and constructed wetlands. *J. Environ. Manag.* **2017**, *195*, 133–139. [CrossRef]
50. Rozman, K.K.; Doull, J.; Hayes, W.J. Dose, time, and other factors influencing toxicity. In *Handbook of Pesticide Toxicology*, 2nd ed.; Krieger, R.I., Krieger, W.C., Eds.; Academic Press: New York, NY, USA, 2001; pp. 1–93.
51. Hodgson, E. Metabolic interactions of pesticides. In *Pesticide Biotransformation and Disposition*, 1st ed.; Hodgson, E., Ed.; Academic Press: New York, NY, USA, 2012; pp. 149–178.
52. Puma, L.G.; Puddu, V.; Toepfer, B. Photocatalytic oxidation of multicomponent mixtures of estrogens (estrone (E1), 17βestradiol(E2), 17α-ethynylestradion (EE2) and estriol (E3)) under UVA and UVC radiation: Photon absorption, quantum yields and rate constants independent of photon absorption. *Appl. Catal. B* **2010**, *99*, 388–397.
53. Bhavsar, K.; Labhane, P.; Huse, V.; Dhake, R.; Sonawane, G. Activated carbon immobilized WO_3 nanocuboids: Adsorption/photocatalysis synergy for the enhanced removal of organic pollutants. *Inorg. Chem. Commun.* **2020**, *121*, 108215. [CrossRef]
54. Singh, M.; Sinha, I. Halide perovskite-based photocatalysis systems for solar-driven fuel generation. *Sol. Energy* **2020**, *208*, 296–311. [CrossRef]
55. Nowak, A.P.; Trzciński, K.; Szkoda, M.; Karczewski, J.; Gazda, M.; Lisowska-Oleksiak, A. A negative effect of carbon phase on specific capacity of electrode material consisted of nanosized bismuth vanadate embedded in carbonaceous matrix. *Synth. Met.* **2019**, *257*, 116168. [CrossRef]
56. Giovannetti, R.; D'Amato, C.A.; Zannotti, M.; Rommozzi, E.; Gunnella, R.; Minicucci, M.; Di Cicco, A. Visible light photoactivity of polypropylene coated Nano-TiO_2 for dyes degradation in water. *Sci. Rep.* **2016**, *5*, 17801. [CrossRef] [PubMed]
57. Li, J.; Yu, X.; Zhu, Y.; Fu, X.; Zhang, Y. 3D-2D-3D BiOI/porous g-C_3N_4/graphene hydrogel composite photocatalyst with synergy of adsorption-photocatalysis in static and flow systems. *J. Alloy. Compd.* **2021**, *850*, 156778. [CrossRef]
58. Nefzi, C.; Souli, M.; Cuminal, Y.; Kamoun-Turki, N. Effect of substrate temperature on physical properties of Cu2FeSnS4 thin films for photocatalysis applications. *Mater. Sci. Eng. B* **2020**, *254*, 114509. [CrossRef]

59. Dudita, M.; Bogatu, C.; Enesca, A.; Duta, A. The influence of the additives composition and concentration on the properties of SnOx thin films used in photocatalysis. *Mater. Lett.* **2011**, *65*, 2185–2189. [CrossRef]
60. Enesca, A.; Andronic, L.; Duta, A. The influence of surfactants on the crystalline structure, electrical and photocatalytic properties of hybrid multi-structured (SnO_2, TiO_2 and WO_3) thin films. *Appl. Surf. Sci.* **2012**, *258*, 4339–4346. [CrossRef]
61. Pedanekar, R.; Shaikh, S.; Rajpure, K. Thin film photocatalysis for environmental remediation: A status review. *Curr. Appl. Phys.* **2020**, *20*, 931–952. [CrossRef]
62. Qin, L.; Chen, Q.; Lan, R.; Jiang, R.; Quan, X.; Xu, B.; Zhang, F.; Jia, Y. Effect of Anodization parameters on morphology and photocatalysis properties of TiO_2 nanotube arrays. *J. Mater. Sci. Technol.* **2015**, *31*, 1059–1064. [CrossRef]
63. Abazari, R.; Sanati, S.; Saghatforoush, L.A. A unique and facile preparation of lanthanum ferrite nanoparticles in emulsion nanoreactors: Morphology, structure, and efficient photocatalysis. *Mater. Sci. Semicond. Process.* **2014**, *25*, 301–306. [CrossRef]
64. Liang, H.; Li, T.; Liu, H. 3-D hierarchical Ag/ZnO@CF for synergistically removing phenol and Cr(VI): Heterogeneous vs. homogeneous photocatalysis. *J. Colloid. Interf. Sci.* **2020**, *558*, 85–94. [CrossRef] [PubMed]
65. Duan, Z.; Zhu, Y.; Hu, Z.; Zhang, J.; Liu, D.; Luo, X.; Gao, M.; Lei, L.; Wang, X.; Zhao, G. Micro-patterned $NiFe_2O_4$/Fe–TiO_2 composite films: Fabrication, hydrophilicity and application in visible-light-driven photocatalysis. *Ceram. Int.* **2020**, *46*, 27080–27091. [CrossRef]
66. Momeni, M.; Saghafian, H.; Golestani-Fard, F.; Barati, N.; Khanahmadi, A. Effect of SiO_2 addition on photocatalytic activity, water contact angle and mechanical stability of visible light activated TiO2 thin films applied on stainless steel by a sol gel method. *Appl. Surf. Sci.* **2017**, *392*, 80–87. [CrossRef]
67. Pinto, M.; Salgado, R.; Laia, C.A.T.; Cooper, W.J.; Sontag, G.; Burrows, H.D.; Branco, L.C.; Vale, C.; Noronha, J. The effect of chloride ions and organic matter on the photodegradation of acetamiprid in saline waters. *J. Photochem. Photobiol. A Chem.* **2018**, *360*, 117–124. [CrossRef]
68. Duta, A.; Enesca, A.; Bogatu, C.; Gyorgy, E. Solar-active photocatalytic tandems. A compromise in the photocatalytic processes design. *Mater. Sci. Semicond. Process.* **2016**, *42*, 94–97. [CrossRef]
69. Enesca, A.; Isac, L.; Duta, A. Charge carriers injection in tandem semiconductors for dyes mineralization. *Appl. Catal. B Environ.* **2015**, *162*, 352–363. [CrossRef]
70. Gao, S.P. Crystal structures and band gap characters of h-BN polytypes predicted by the dispersion corrected DFT and GW method. *Solid State Commun.* **2012**, *152*, 1817–1820. [CrossRef]
71. Mise, T.; Nakada, T. Low temperature growth and properties of Cu–In–Te based thin films for narrow bandgap solar cells. *Thin Solid Films* **2010**, *518*, 5604–5609. [CrossRef]
72. Carvalho, K.T.G.; Lopes, O.F.; Ribeirox, C. ZnO:$ZnWO_4$ heterostructure with enhanced photocatalytic activity for pollutant degradation in liquid and gas phases. *J. Alloy. Compound.* **2019**, *797*, 1299–1309. [CrossRef]
73. Testoni, G.O.; Amoresi, R.A.C.; Perazollix, L.A. Increased photocatalytic activity induced by TiO_2/Pt/SnO_2 heterostructured films. *Solid State Sci.* **2018**, *76*, 65–73. [CrossRef]
74. Dostanić, J.; Lončarević, D.R.; Đorđević, V.; Ahrenkiel, S.P.; Nedeljković, J.M. The photocatalytic performance of silver halides—Silver carbonate heterostructures. *J. Photochem. Photobiol. A Chem.* **2017**, *336*, 1–7. [CrossRef]
75. Nazim, S.; Kousar, T.; Warsi, M.F. New graphene-CoxZn1−xFe_2O_4 nano-heterostructures: Magnetically separable visible light photocatalytic materials. *Ceram. Int.* **2016**, *42*, 7647–7654. [CrossRef]
76. Baneto, M.; Enesca, A.; Mihoreanu, C.; Lare, Y.; Jondo, K.; Napo, K.; Duta, A. Effects of the growth temperature on the properties of spray deposited $CuInS_2$ thin films for photovoltaic applications. *Ceram. Int.* **2015**, *41*, 4742–4749. [CrossRef]
77. Scanlon, D.O.; Dunnill, C.W.; Buckeridge, J.; Shevlin, S.A.; Logsdail, A.J.; Woodley, S.M.; Catlow, C.R.A.; Powell, M.J.; Palgrave, R.G.; Parkin, I.P.; et al. Band alignment of rutile and anatase TiO_2. *Nat. Mater.* **2013**, *12*, 798–801. [CrossRef] [PubMed]